Icarus 199 (2009) 264–272

Contents lists available at ScienceDirect

Icarus

www.elsevier.com/locate/icarus

Atomic oxygen distribution in the Venus mesosphere from observations of O_2 infrared airglow by VIRTIS-Venus Express

Jean-Claude Gérard [a,*], Adem Saglam [a], Giuseppe Piccioni [b], Pierre Drossart [c], Frank Montmessin [d], Jean-Loup Bertaux [d]

[a] Laboratoire de Physique Atmosphérique et Planétaire, Université de Liège, 17, allée du 6 août – B5c, Sart Tilman, B-4000 Liège, Belgium
[b] IASF-INAF, Roma, Italy
[c] LESIA, Observatoire de Paris, Meudon, France
[d] Service d'aéronomie du CNRS, Verrières-le-Buisson, and Université de Versailles Saint-Quentin-en-Yvelines, France

ARTICLE INFO

Article history:
Received 7 May 2008
Revised 9 September 2008
Accepted 20 September 2008
Available online 12 November 2008

Keywords:
Venus
Infrared observations
Atmospheres, composition
Atmospheres, dynamics

ABSTRACT

This VIRTIS instrument on board Venus Express has collected spectrally resolved images of the Venus nightside limb that show the presence of the (0,0) band of the ${}^1\Delta_g \rightarrow {}^3\Sigma_g$ infrared atmospheric system of O_2 at 1.27 μm. The emission is produced by three-body recombination of oxygen atoms created by photodissociation of CO_2 on the dayside. It is consistently bright so that emission limb profiles can be extracted from the images. The vertical distribution of $O_2({}^1\Delta_g)$ may be derived following Abel inversion of the radiance limb profiles. Assuming photochemical equilibrium, it is combined with the CO_2 vertical distribution to determine the atomic oxygen density. The uncertainties on the O density caused by the Abel inversion reach a few percent at the peak, increasing to about 50% near 120 km. We first analyze a case when the CO_2 density was derived from a stellar occultation observed with the SPICAV spectrometer simultaneously with an image of the O_2 limb airglow. In other cases, an average CO_2 profile deduced from a series of ultraviolet stellar occultations is used to derive the O profile, leading to uncertainties on the O density less than 30%. It is found that the maximum O density is generally located between 94 and 115 km with a mean value of 104 km. It ranges from less than 1×10^{11} to about 5×10^{11} cm^{-3} with a global mean of 2.2×10^{11} cm^{-3}. These values are in reasonable agreement with the VIRA midnight oxygen profile. The vertical O distribution is generally in good agreement with the oxygen profile calculated with a one-dimensional chemical-diffusive model. No statistical latitudinal dependence of the altitude of the oxygen peak is observed, but the maximum O density tends to decrease with increasing northern latitudes. The latitudinal distribution at a given time exhibits large variations in the O density profile and its vertical structure. The vertical oxygen distribution frequently shows multiple peaks possibly caused by waves or variations in the structure of turbulent transport. It is concluded that the O_2 infrared night airglow is a powerful tool to map the distribution of atomic oxygen in the mesosphere between 90 and 115 km and improve future Venus reference atmosphere models.

1. Introduction

Atomic oxygen is the most abundant constituent in the Venus nightside thermosphere between ∼140 km and 170 km. It is produced by photodissociation of CO_2 and, to a minor extent, CO and O_2 on the dayside. The O density was measured with the Pioneer Venus Orbiter Neutral Mass Spectrometer (PV-ONMS) from December 1978 to August 1980 at solar maximum (F10.7 index ∼200 at 1AU) (Niemann et al., 1980). All local times were covered within a few degrees of the periapsis latitude (16°N) with periapsis altitudes ranging between 141 and 250 km. Additional data were collected during the orbiter re-entry at local times from 18.5 to 4.5 h when the F10.7 cm solar flux index was about 150 (Kasprzak et al., 1993). The oxygen vertical distribution was shown to be in diffusive equilibrium above ∼130 km, as expected from the altitude of the homopause. Wave-like perturbations have been observed with the ONMS along in the orbital path in the thermosphere (Kasprzak et al., 1988, 1993) with horizontal wavelengths in the range 100–600 km. These structures were shown to be consistent with gravity waves propagating upward into the lower thermosphere from a low as 80 km (Mayr et al., 1988).

Most photochemical models (e.g., Yung and DeMore, 1982; Krasnopolsky and Parshev, 1983) considered daytime or globally averaged conditions but did not specifically address the oxygen nightside photochemistry. The vertical distribution of O atoms in the nightside thermosphere and mesosphere was modelled by

* Corresponding author.
E-mail address: jc.gerard@ulg.ac.be (J.-C. Gérard).

0019-1035/$ – see front matter
doi:10.1016/j.icarus.2008.09.016

Massie et al. (1983) using a one-dimensional chemical-diffusive model. The temperature and eddy diffusion profiles were prescribed as well as the downward (vertical) flux of O and N atoms through the upper boundary. Hydrostatic equilibrium was assumed for CO_2 and its vertical flux was set to zero. The calculated O density profile at midnight peaked at 105 km reaching a value $\sim 2.4 \times 10^{11}$ cm^3. The Venus International Reference Atmosphere (VIRA) (Keating et al., 1985) is largely based on the ONMS measurements above 140 km. Density profiles were extended from the diffuse equilibrium dominated regime above the homopause down into the homosphere. For this purpose, empirical formulae were used to provide a transition through the homopause region. In the case of atomic oxygen, the density profiles were smoothly connected to the distribution calculated by Massie et al. (1983). Instead, the widely used VTS3N empirical model by Hedin et al. (1983) does not provide realistic O densities below about $\sim$120 km since the O density profile was extrapolated downward assuming hydrostatic equilibrium and shows no peak density. The role played by the solar to antisolar (SSAS) circulation and the zonal circulation on the global composition was analyzed with a three-dimensional model by Bougher and Borucki (1994). They also calculated the atomic oxygen distribution on both the day and the night sides and studied the sensitivity of the airglow morphology to solar activity and strength of turbulent transport. In summary, the atomic oxygen density is only poorly known and loosely constrained in the region where it reaches its largest values, around 110 km.

Connes et al. (1979) first detected the O_2 airglow emission at 1.27 mm from both the day and the night sides of Venus. Ground-based spatially resolved observations (Allen et al., 1992; Crisp et al., 1996; Lellouch et al., 1997) showed that the spatial distribution of the O_2 infrared airglow produced by three-body recombination, of O atoms is quite variable and time dependent, showing enhanced regions usually 1000–2000 km wide. These rapidly changing bright areas occur most frequently at low latitudes between midnight and 0300 local time. Using the Near-Infrared Mapping Spectrometer (NIMS) on board the Galileo spacecraft, Drossart et al. (1993) observed a large enhancement of the 1.27 μm emission at a latitude of 40° S, over a spatial area about 100 km wide. The variability of the airglow distribution has been analyzed in terms of apparent motion of gas masses transported by horizontal (meridional and zonal) winds (Hueso et al., 2008). Images obtained with the Infrared Thermal Imaging Spectrometer (VIRTIS) on board Venus Express show that the variability is of short term with most of the details changing over 30-min but with the large structures usually surviving at least through 1–2 h. An apparent jet typically 30 $m\,s^{-1}$ is commonly observed in the prograde (duskward) direction and the mean meridional apparent motion is 20–5 $m\,s^{-1}$ from the pole to the equator. Gérard et al. (2008a) presented global characteristics of the average O_2 infrared nightglow in the southern hemisphere observed with VIRTIS over an 11-month period of low solar activity. They showed that the distribution is inhomogeneous with an enhanced region $\sim$3 MegaRayleighs (MR) located near the midnight meridian at low latitude. The hemispherically averaged nadir brightness of 1.3 MR, was shown to be compatible with the dayside supply of O atoms if approximately 50% of the dayside O production is carried to the nightside by the subsolar to antisolar global circulation.

Limb profiles of the $O_2(^1\Delta)$ emission at 1.27 μm have recently been obtained with VIRTIS (Drossart et al., 2007a; Gérard et al., 2008a; Piccioni et al., 2008). Drossart et al. (2007b) showed the airglow peaks at $\sim$97 km. Gérard et al. (2008a) compared two limb profiles located 12° of latitude apart obtained on the same limb image. They showed that the peak altitude of both profiles remained close to 96 km, but the peak brightness differed by more than 30% in spite of the small distance separating the two profiles. They compared the limb profiles to those obtained with a one-dimensional chemical-diffusive model where the strength of the eddy diffusion coefficient and the downward flux of O atoms were left as free parameter. The found that the eddy diffusion was less than earlier determinations by Von Zahn et al. (1980) and Gérard et al. (1981), in agreement with the analysis based on the vertical distribution of the nitric oxide nightglow by Gérard et al. (2008b). The peak altitude and intensity were satisfactorily reproduced by the model, but the width of the airglow layer was narrower than in the numerical simulation. This difference suggested that vertical downward winds may play a role in redistributing oxygen atoms. Piccioni et al. (2008) illustrated the variability and the complexity of the observed airglow limb profiles. They showed that the altitude and brightness of the emission peak sometimes varies systematically with latitude. They also argued that a secondary peak possibly generated by upward propagating gravity waves is sometimes observed above 100 km.

In this study, we show that recent VIRTIS limb observations at 1.27 μm may be used to investigate the O distribution on the nightside in the 90–110 km region. In particular, we examine how $O_2(^1\Delta)$ emission limb profiles may be used to probe the distribution of atomic oxygen in the airglow layer by inverting the limb profile and applying current knowledge of the oxygen chemistry on the Venus nightside. We discuss the sources of uncertainties on the absolute O density using CO_2 profiles derived from stellar absorption observations obtained with the SPICAV spectrometer also on board Venus Express. We present latitudinal cross sections indicating that the vertical distribution of O atoms varies with latitude. An overview of the statistical distribution of the altitude and number density of the O peak concentration is derived from the analysis of several hundreds of limb profiles of the O_2 infrared emission. Finally, we discuss how oxygen profiles derived from the airglow may be used in future models of the Venus upper mesosphere and lower thermosphere.

2. VIRTIS limb observations and profile inversion

Venus Express is on an elliptical orbit with a period of 24 h, an apocenter at 66,000 km and a pericenter at 250 km, located at 80° N (Svedhem et al., 2007; Titov et al., 2006). It is fixed in inertial space so that it precesses in local time and covers a full cycle in a Venus year. Spectral images of the planetary limb have been obtained with VIRTIS in the spectral imaging M mode. The VIRTIS instrument and its modes of operation have been described by Drossart et al. (2007a) and Piccioni et al. (2008). In brief, VIRTIS-M provides spectral cubes between 0.25 and 5 μm at a spectral resolution $R \sim 200$. Each spectral channel is $\sim$9.5 nm wide in the region of the O_2 IR emission. A spatial scan, covering a 64 mrad × 64 mrad field of view, is generally obtained in about 10 min using a scanning mirror. The 0.25 mrad pixel size of the VIRTIS-M detector projected on Venus limb provides a spatial resolution of 1.9 km for a spacecraft distance of 7500 km, a value which is typical of a VIRTIS observation at 40° N. In this study, we only use images where the field of view intercepts the limb from a distance of less than 12000 km. A total of 95 limb images at 1.27 μm have been analyzed, covering a period extending from June 2006 to November 2007. The F10.7 daily solar activity index averaged over the days when observations were collected was 72×10^{-22} $W\,m^{-2}\,Hz^{-1}$. Thermal radiation from the lower atmosphere produces a background contribution when observing at the nadir (Gérard et al., 2008a). Analysis of the spectral cubes in the vicinity of 1.27 μm at the limb indicates that this contribution is very small for altitudes of the tangent point above $\sim$85 km and thermal background corrections are negligible above 90 km (Piccioni et al., 2008). Fig. 1a shows an example of limb profiles observed on VEX orbit 383 (May 9, 2007) at 20° N and 0000 local time. The emission shows a peak reaching 40 MR at 98 km, an altitude close to the

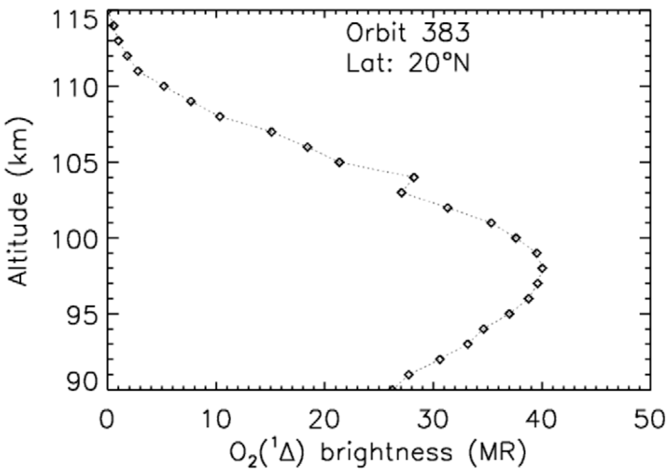

(a)

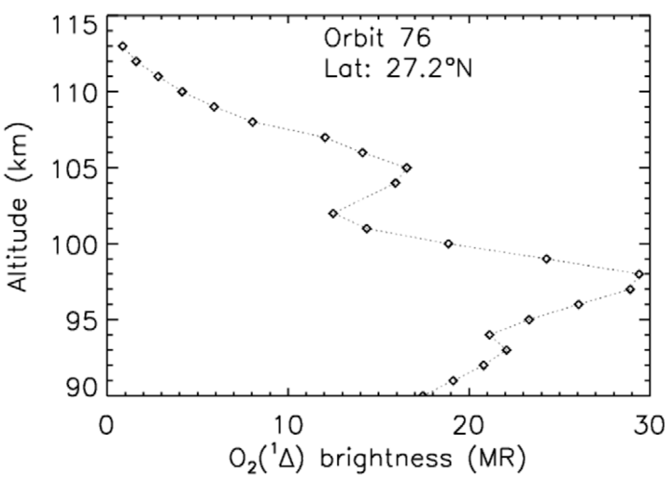

(b)

Fig. 1. Examples of intensity limb profiles of the $O_2(^1\Delta)$ nightglow emission obtained from VIRTIS-M images: (a) orbit 383 (May 9, 2007) at 0000 LT, (b) orbit 76 (July 6, 2006) at 0130 LT.

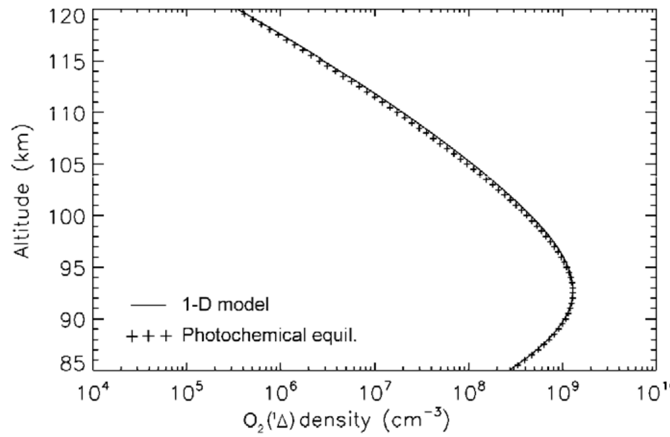

Fig. 2. Vertical distribution of the $O_2(^1\Delta)$ density calculated with the one-dimensional chemical-diffusive model (solid line) and in the photochemical equilibrium approximation (+++).

mean altitude of the peak observed in the northern hemisphere with VIRTIS (Drossart et al., 2007a, 2007b; Gérard et al., 2008a; Piccioni et al., 2008). As was noticed by Drossart et al. (2007b), the observed topside scale height of the O_2 emission profile ($\sim$3 km) is less than expected from a uniformly mixed atmosphere in hydrostatic equilibrium. In the case of the 1.27 µm airglow produced by recombination of O atoms flowing downward in the homosphere toward a chemical sink region, Stewart et al. (1980) showed that the analytical solution indicates that the topside scale height of the O density varies as $1/K$. Consequently, for a K coefficient varying as the inverse square root of the CO_2 density, the O scale height is expected to vary as the square root of the CO_2 density. Since the O_2 airglow volume emission rate above the region of significant collisional quenching is proportional to the $[O]^2 \times [CO_2]$ product, the airglow scale height above the peak altitude is expected to be close to half the value of the CO_2 scale height, that is on the order of 1.6 km at 2400 LT at the equator. Comparison with airglow limb profiles indicates that the observed scale height is typically about 2.5 km, that is larger than predicted by this simple model. Fig. 1b shows a limb profile obtained during orbit 76 (July 6, 2006) at 27.2° N, at 0130 LT. In this case, the width of the main (lower) emission layer is less than in the previous example and a secondary peak is observed at 105 km. The presence and the characteristics of such secondary peaks above 100 km have been discussed by Piccioni et al. (2008). They were found to be most frequent at northern latitudes between 45° and 75° and have been interpreted as possible signatures of gravity waves vertically redistributing the oxygen concentration.

Limb profiles such as those presented in Fig. 1 may be inverted to obtain the $O_2(^1\Delta)$ vertical distribution. We assume the distribution to be spherically symmetric and we use an integral inversion algorithm based on the properties of the Abel method. The validity of the assumption of spherical symmetry will be discussed later. We calculate the inverse Abel transform by approximating the inverse profile with cubic splines whose parameters are determined so that they minimize the following expression:

$$S = (1-\lambda)\int \left(cA(n) - E\right)^2 dz + \lambda R,$$

where $A(n)$ is the Abel transform of the seeked n density, E the observed emission profile and R is a regularization functional chosen to be

$$R = \int \left(\frac{d^2n}{dz^2}\right)^2 dz,$$

where λ is a parameter that controls the relative importance of the two terms and is chosen so that the first term, i.e. the data fidelity term, will end up being equal to the estimated variance of the noise. The role of the regularization functional is to give a smoother inverse profile depending on the size of λ. The c coefficient is present in the fidelity term for physical unit compatibility. To convert emission rate into $O_2(^1\Delta)$ column densities a radiative lifetime of 4300 s (Miller et al., 2001) has been adopted. The $O_2(^1\Delta)$ densities derived from Fig. 1 show peak values of 3×10^9 cm^{-3} and 1×10^{10} cm^{-3}, corresponding to mixing ratio of 1.3×10^{-6} and 4×10^{-6}, respectively.

To derive O densities from the $O_2(^1\Delta)$ distribution, we assume that the distribution of excited O_2 molecules is primarily controlled by photochemistry. The validity of the assumption may be tested by comparing the $O_2(^1\Delta)$ radiative lifetime with the characteristic time for vertical transport. The importance of vertical transport in the $O_2(^1\Delta)$ vertical distribution has been tested using the one-dimensional chemical-diffusive model (Gérard et al., 2008b) described below. In these simulations, the $O_2(^1\Delta)$ vertical distribution has been calculated without the vertical transport term due to molecular and eddy diffusion and with both transport terms using a K coefficient equal to $2 \times 10^{13}/n^{1/2}$ cm^2 s^{-1} and a downward vertical wind velocity $w \sim 0.1$ m s^{-1} compatible with the three-dimensional model by Bougher and Borucki (1994). The comparison of the two runs presented in Fig. 2 indicates that the two solutions are identical. It is thus concluded that $O_2(^1\Delta)$

molecules are in photochemical equilibrium below 120 km, and hence that Eq. (4) given below adequately describes the relationship between the $O(^3P)$ and the $O_2(^1\Delta)$ number densities. In photochemical equilibrium, a balance is established between chemical production:

$$O + O + M \rightarrow O_2(^1\Delta) + M \tag{1}$$

and loss:

$$O_2(^1\Delta) \rightarrow O_2(^3\Sigma) + 1.27\ \mu m \tag{2}$$

or:

$$O_2(^1\Delta) + M \rightarrow O_2(^3\Sigma) + M. \tag{3}$$

Accordingly, the O density is given by:

$$[O] = \left\{ [O_2(^1\Delta)] \frac{A + C[M]}{k\varepsilon[M]} \right\}^{1/2}, \tag{4}$$

where k is the rate coefficient of reaction (1) equal to $2.5 \times 10^{-32}\ cm^6\,s^{-1}$, which is obtained by multiplying the value measured at 200 K by Campbell and Gray (1973) with N_2 and O_2 as third bodies by a factor 2.5 to account for the higher reactivity of CO_2 (Nair et al., 1994; Slanger et al., 2006). A is the Einstein coefficient of the 1.27 µm transition, ε the efficiency of the production of $O_2(^1\Delta)$ in reaction (1) and C is the quenching coefficient of $O_2(^1\Delta)$ by major species assumed to be dominated by CO_2. For the quenching coefficient C of reaction (3), we use the value of $2 \times 10^{-20}\ cm^3\,s^{-1}$ recommended by Sander et al. (2003), which is actually an upper limit. With these values, the rates of collisional and the radiative deactivation are equal at ∼91 km. Approximately 80% of the $O_2(^1\Delta)$ molecules emit a 1.27 µm photons at the altitude of the emission peak. Consequently, even if the C coefficient is set to zero, the derived O distribution only differs by ∼10% at the altitude of the airglow peak. The value of ε has been extensively discussed in the literature. Krasnopolsky (1986) argued that in three-body recombination of O atoms, only a small percentage of the O_2 molecules are formed directly in the $^1\Delta_g$ state. He suggested that recombination of O atoms proceeds through the weakly bond $^5\Pi_g$ state which is the common precursor to the five metastable states of O_2. Bates (1988) estimated that 7% of the oxygen atom associations directly produce the $^1\Delta$ state. The net efficiency of $O_2(^1\Delta)$ is now estimated to be close to unity, since the $^1\Delta_g$ state is populated by cascades from upper lying O_2 states (Krasnopolsky, 1986; Crisp et al., 1996). We use an efficiency value $\varepsilon = 0.75$ suggested by Crisp et al. (1996) on the basis of the constraints derived from the O_2 infrared Earth airglow. Processes other than reaction (1) have been proposed as possible sources of $^1\Delta$ molecules in the Venus nightside upper atmosphere. This was the case for catalytic cycles involving OH or Cl, but the yield of $^1\Delta$ molecules by these processes appears to be negligibly small (Leu and Yung, 1987) and it now appears that reaction (1) alone significantly contributes to the observed airglow intensity.

As shown in formula (4), knowledge of the vertical distribution of the total number density is necessary to derive the oxygen distribution from the infrared airglow profiles. As discussed earlier, the number densities of the main constituents are given by Hedin et al. (1983) in the VTS3N code. Since CO_2 accounts for 96.5% of the total density below the homopause, the [M] value is obtained by multiplying the CO_2 density by 1.035. More direct measurements of the CO_2 density have been obtained from stellar occultation observations performed on the Venus nightside with the SPICAV spectrometer (Bertaux et al., 2007). The method consists in observing a bright UV star outside and through the venusian atmospheric shell in order to infer the amount of CO_2 molecules (and aerosols) which possess a prominent electronic transition between 120 and 200 nm and which thus cause a quantifiable dimming of the stellar beam in that spectral range (Yoshino et al., 1996; Parkinson et al., 2003). The method, as for any occultation technique, is self-calibrated since absolute quantities are deduced from relative measurements, that is the ratio of spectra recorded outside and through the atmosphere (commonly referred as to transmissions). An improved version of the inversion routine presented in Montmessin et al. (2006a, 2006b) and Quémerais et al. (2006) has been used. Inverting occultation data only requires consideration of the simple Beer–Lambert's law, expressing that source attenuation scales exponentially with opacity. Spectral inversion is performed independently for every altitude with a least-square fitting technique (Levenberg–Marquardt) to infer the number of CO_2 molecules and the aerosol opacity integrated over the line of sight. CO_2 local density is a by-product of our temperature profile inversion routine. For every level, the temperature is adjusted so as to match the observed line-of-sight integrated number of CO_2 molecules with the constraint of hydrostatic equilibrium and perfect gas law. The routine starts at the profile top (near 140 km) where a first temperature guess is made. Temperature is then sequentially retrieved in the layer immediately below down to 85 km where stellar signal is lost because of the upper venusian haze.

During VEX orbit 383, an image of the limb was taken while bright UV star HR6165 was occulted at the same time by the Venus atmosphere. Therefore, the vertical distribution of CO_2 was determined between 140 and 85 km while the SPICAV line of sight moved from 29° N to 32° N at midnight. The corresponding data points are plotted in Fig. 3 as red diamonds. The CO_2 density from the VIRA model at midnight is represented by the black solid line for comparison. The SPICAV values are larger by a factor of about 2 at 130 km and lower than VIRA by also a factor of 2 at 85 km. The two curves cross near 105 km, in the region of the maximum oxygen density. At the altitude of the airglow peak, near 97 km, the differences are on the order of 30%. An exponential fit through the SPICAV data points is shown by the red solid line. We note that the scale height of the SPICAV observation is slightly different from the VIRA points and correspond to a warmer atmosphere than in the VIRA model. Discrepancies with the VIRA model temperatures in the 90 to 120 km region were pointed out by Bertaux et al. (2007) who found that temperatures deduced from SPICAV occultations are systematically larger than those given in the VIRA model. Analysis of additional stellar occultations confirms that the nightside temperature in the upper mesosphere and lower thermosphere is about 10 to 20 K above the VIRA values. A compilation of CO_2 measurements between 77 and 140 km based on additional stellar occultations is also shown in Fig. 3 (green diamonds). These observations were performed between 50° S and 40° N at local times ranging from 2000 to 0400 LT. As was the case for orbit 383, most of the measured densities exceed the VIRA values above 100 km while VIRA overestimates CO_2 below this altitude. The O_2 IR airglow peak is thus generally located in a region where the CO_2 density is satisfactorily predicted by the VIRA model. The 1-σ scatter among the SPICAV data points is on the order of a factor of two, mostly reflecting actual variability of CO_2 rather than observational uncertainties.

3. Atomic oxygen vertical distribution

Fig. 4 shows the atomic oxygen density derived from the limb profiles presented in Fig. 1, following Abel integral inversion and application of Eq. (4). The CO_2 density values were obtained using the exponential fitted through the SPICAV data points of Fig. 3. In the Abel inversion, we assume a spherical symmetry for the density profiles. However, the global map of $O_2(^1\Delta)$ nightglow emission (Gérard et al., 2008a) and individual nadir images (Hueso et al., 2008; Piccioni et al., 2008) shows that it is not quite the case.

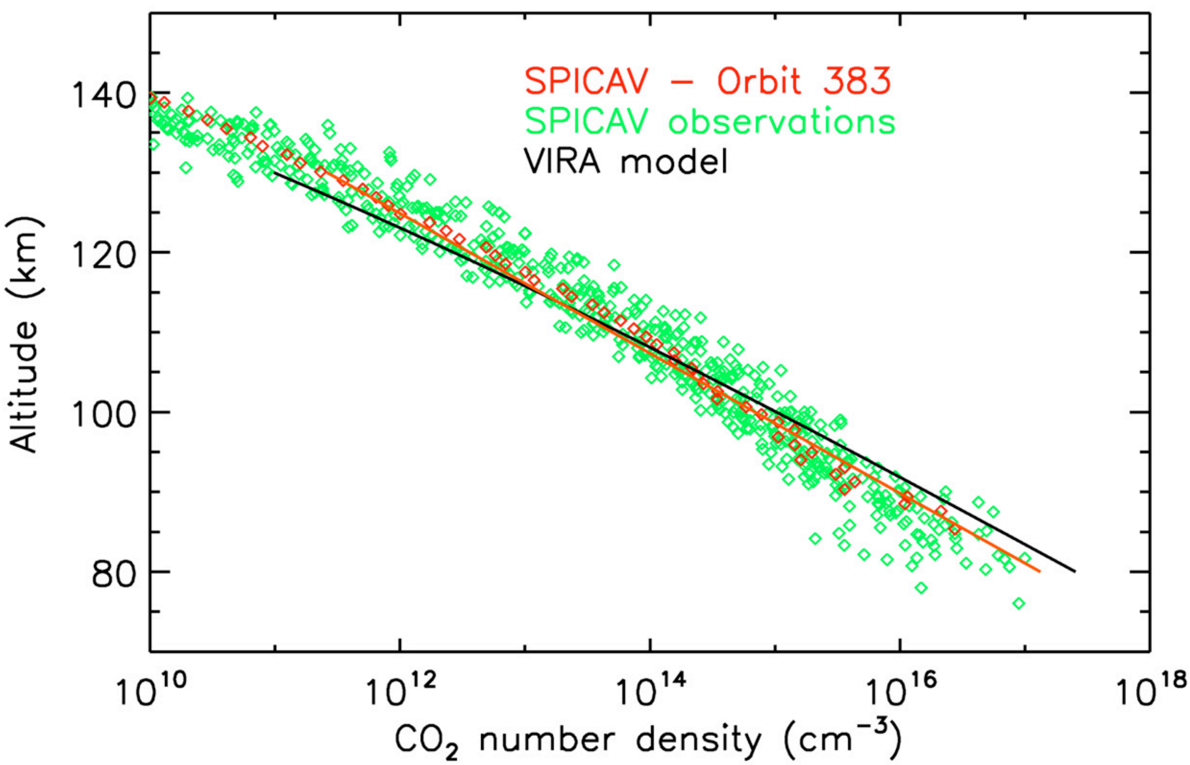

Fig. 3. Altitude distribution of the CO_2 density derived from stellar occultation measurements with the SPICAV UV spectrometer for orbit 383 (red diamonds) and for all available SPICAV nightside profiles (green diamonds). The fits through the data points of orbit 383 and through all data points cannot be distinguished from each other and are represented by the red solid line. The equatorial distribution from VIRA at 0000 LT is also shown for comparison (black solid line).

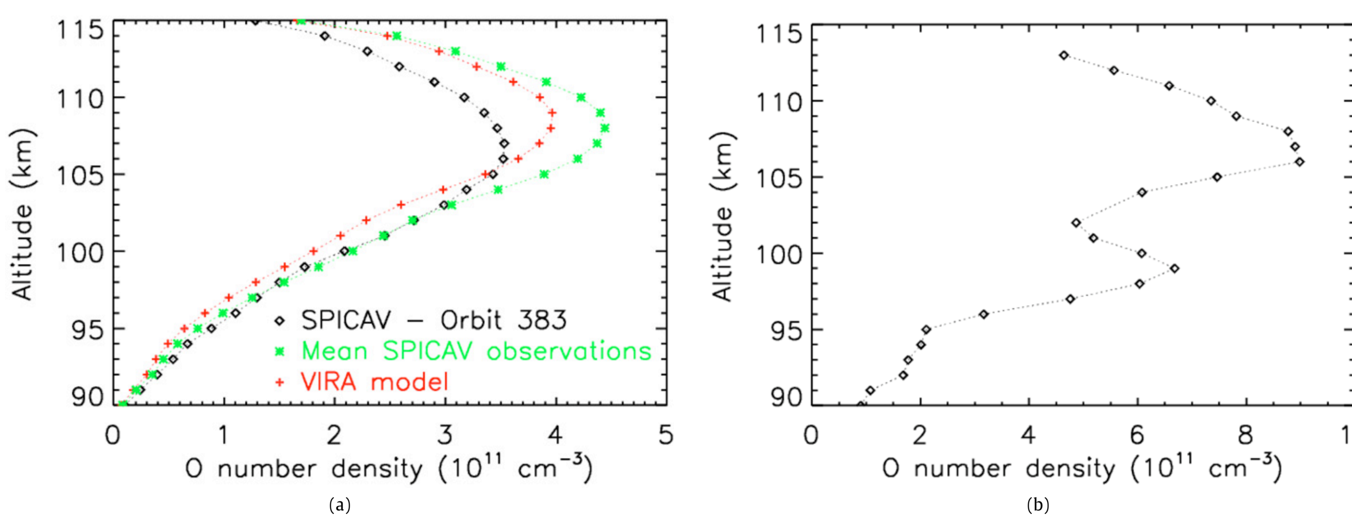

Fig. 4. Vertical distribution of atomic oxygen derived from the $O_2(^1\Delta)$ emission following integral inversion and application of Eq. (4). (a) Orbit 383. The three O profiles were obtained using different CO_2 distributions: values derived during the concurrent stellar occultation by SPICAV (diamonds), fit through all occultation data points of Fig. 3 ($***$) and the nightside VIRA profile (+++). (b) Same for orbit 76 using the CO_2 profile fitted through all the occultation data points of Fig. 3.

This assumption introduces some errors during the inversion. Significant discrepancies arise especially one scale height below the $O_2(^1\Delta)$ peak. Actually, the Abel inversion is valid in the regions of local spherical symmetry of the density profiles. The length of integration gives an estimate of the validity of this assumption. It is defined as the length of the region measured along the line of sight out of which the intensity reaches values less than e^{-1} times the peak intensity. For a profile showing an exponential decay it may be defined as

$$L(z_{\text{peak}}) = 2\sqrt{2RH}, \tag{5}$$

where L is the length of integration at the peak altitude, R the planet radius and H the scale height of the constituent. For $O_2(^1\Delta)$ emission, with a scale height of about 3 km, this gives a length of integration of about 380 km, corresponding to an angle along a great circle of 3.5°. Consequently, the spherical symmetry assumption at the peak altitude is valid in the absence of longitudinal structure smaller than 3.5° in the latitude and local time region considered. One scale height below the peak altitude, the length of integration is equal to $L(z_{\text{peak}} - H) = 4\sqrt{RH}$. With the previous values, this length of integration is approximately equal to 540 km corresponding to an angle of 5° so that this length becomes critical at lower altitudes, where the relative errors can reach up to

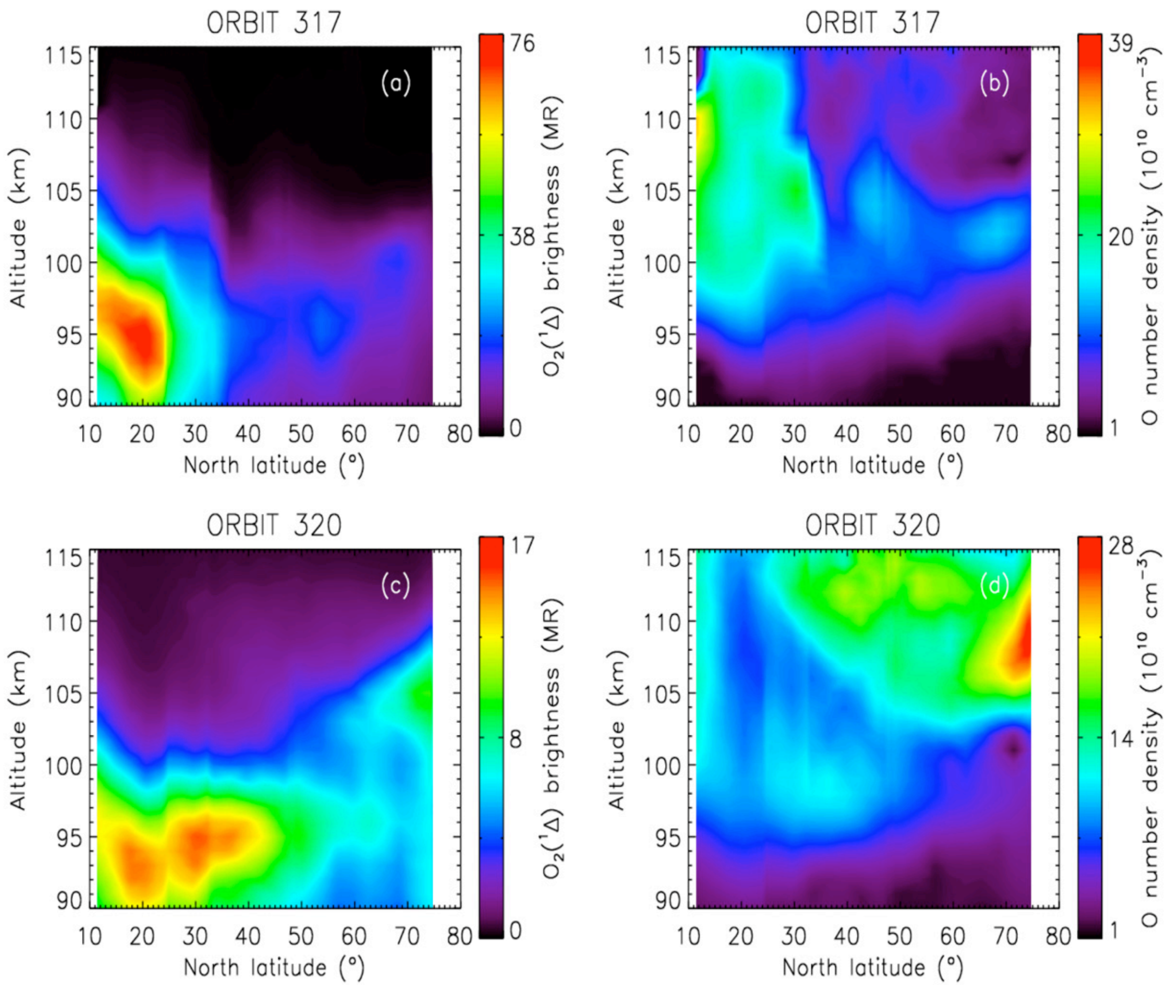

Fig. 5. Latitudinal distribution of the O_2 1.27 μm limb intensity and O density derived from inversion of the VIRTIS O_2 infrared airglow observations: (a) airglow limb profile and (b) O number density from orbit 317 (March 4, 2007), (c) airglow limb profile and (d) O number density from orbit 320 (March 7, 2007).

50%. While the airglow limb profile at 1.27 μm measured during orbit 383 peaks at 98 km (Fig. 1a), the O density peak in Fig. 4a is located at 107 km where it reaches 3.5×10^{11} cm^{-3}. We note that the outlier point observed on the airglow limb profile at 104 km has no significant counterpart in the O profile as a result of the smoothing procedure in the Abel inversion algorithm. However, the presence of the CO_2 density in the numerator of (4) raises the altitude of the O density peak approximately 9 km above the altitude of the airglow peak. Fig. 4b shows the O density distribution obtained following Abel inversion of the O_2 1.27 μm emission from orbit 76 shown in Fig. 1b. The corresponding O density profile shows a broad peak with a maximum of 9.2×10^{11} cm^{-3} at 106 km. In this case, the lower altitude airglow maximum, although of higher intensity than the upper peak, corresponds to a secondary O maximum of 6.7×10^{11} cm^{-3} at 99 km.

Latitudinal distributions of the O vertical profile may be constructed in the northern hemisphere for those VEX orbits where adjacent VIRTIS images of the night limb were collected. This is the case of orbits 317 (March 4, 2007) and 320 (March 7, 2007) between 10° and 80° N. The data were obtained over a 10 min time span, so that these distributions may be nearly considered as snapshots of the O distribution at 0030 LT. They both reveal features of the nightside oxygen distribution previously unobserved. In Fig. 5a (orbit 317), a bright region of 1.27 μm emission ($\sim$100 MR) is seen at low latitude, as expected from the global distribution of $O_2(^1\Delta)$ emission showing a region of enhanced emission near the equator. The peak altitude drops with increasing northern latitude by $\sim$3 km over a 10° of latitude. At higher latitudes, the peak intensity is dimmer by about a factor of 2 and rises continuously up to 99 km at 80° N. It should be noted that all limb profiles are single-peaked and show a fairly rapid drop above 110 km. The O density is displayed in Fig. 5b and shows a more complex structure. At latitude less than 18° N, the O maximum is at $\sim$108 km. It rapidly gives way to a double-peaked distribution at 20° N, returning back to a single maximum beyond 25° N. A region of lower O density is observed near 40°, corresponding to the sharp edge present in the 1.27 μm airglow. Northward of 42°, the O density peaks between 102 and 107 km. Fig. 5c also shows a low-latitude region of enhanced emission at low altitude with a maximum slowly increasing with latitude but remaining below 97 km up to 70° where a secondary peak, similar to the structure observed in Fig. 1b is present. The corresponding O distribution (Fig. 5d) shows a fairly flat O density profile at $\sim 1 \times 10^{11}$ cm^{-3} up to $\sim$27° N where the main maximum rapidly rises to 111 km, followed by a continuous drop of the peak altitude and a substantial density increase above 70°. It must be stressed that the observed O_2 airglow is the result of the integration of the volume emission rate along the line of sight. Consequently, if the airglow layer is inhomogeneous, a region of enhanced emission at high altitude located in front of or behind the tangent point may appear as a secondary lower altitude peak in the limb profile. Therefore, although these higher altitude features are real, they do not necessarily belong to the same emitting region as the lower altitude peak. The presence of such observational artifacts is expected in regions presenting an abrupt change

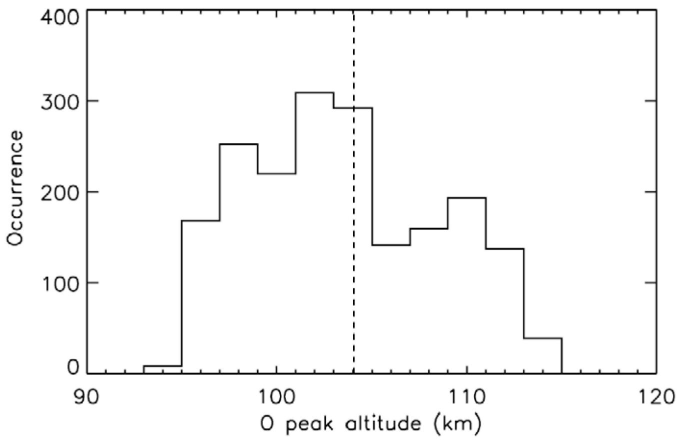

Fig. 6. Histogram of altitude of the atomic oxygen maximum derived from limb images of the O_2 airglow observed with VIRTIS-M. The vertical dashed line indicates the mean value.

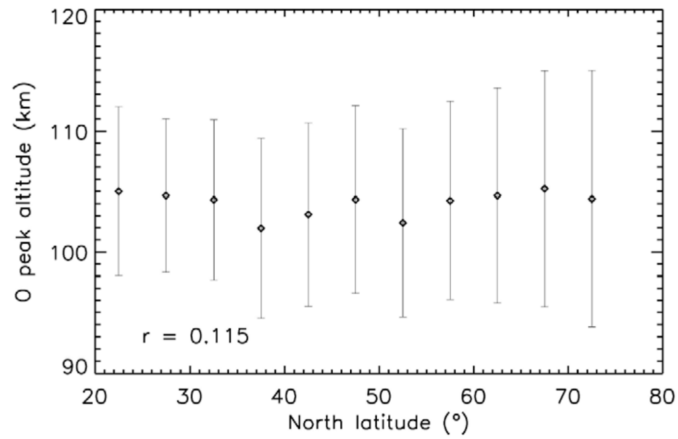

Fig. 8. Latitudinal distribution of the altitude of the O maximum density. The vertical bars show the 1-σ standard deviation of the values in each latitudinal bin.

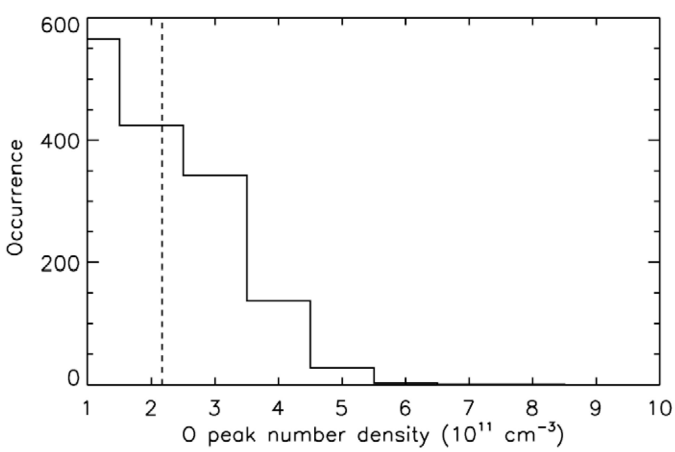

Fig. 7. Histogram of the number density of the atomic oxygen maximum derived from limb images of the O_2 airglow observed with VIRTIS-M. The vertical dashed line indicates the mean value.

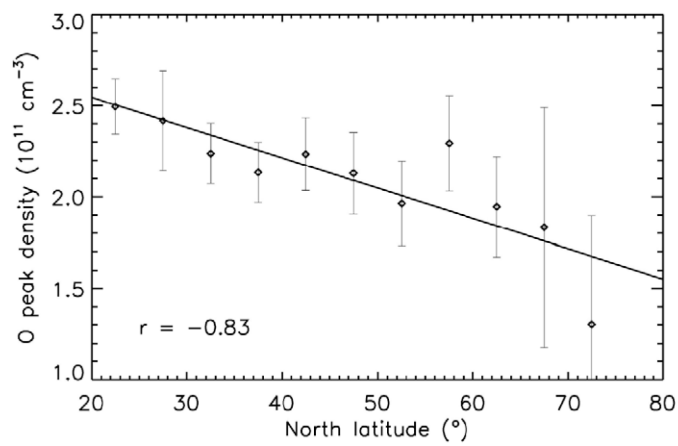

Fig. 9. Latitudinal distribution of the O peak density. The vertical bars show the 1-σ standard deviation of the values in each latitudinal bin and the horizontal dashed line indicates to the mean value. The solid line is the best-fit linear regression through the data points.

in the altitude of the emission peak such as in Fig. 5c where the transition region between 60° and 70° N presents a double peak in the limb profile.

4. Latitudinal distribution of atomic oxygen

We now examine the statistical distribution of the atomic density derived from $O_2(^1\Delta_g)$ emission limb profiles based on the methodology described before. For this purpose, vertical profiles are extracted from the limb images and averaged over 3 degrees of latitude. Each one is inverted and the corresponding atomic oxygen profile is obtained using the mean CO_2 vertical distribution deduced from the SPICAV stellar occultations shown in Fig. 3. A total of 1918 oxygen vertical profiles covering latitudes from 20° to 75° N has been obtained over the June 2006 to November 2007 period. The individual profiles show a great deal of variability both in altitude and oxygen density. To obtain a global view of the variability of oxygen, Figs. 6 and 7 show the histograms of the altitude of the maximum O density and the value of the peak density. In Fig. 6, the data have been grouped into 2-km altitude bins. The distribution is non-Gaussian and extends from 93 to 105 km, with a maximum at 102 km and a mean value of 104 km. The distribution value of the O peak density is represented in Fig. 7 with number density bins 1×10^{11} cm^{-3} wide. The values extend from 2.8×10^{10} to 8.5×10^{11} cm^{-3} with a mean of 2.2×10^{11} cm^{-3}. Peak densities larger that 5.5×10^{11} cm^{-3} represent only 0.3% of the all observations.

We seek for a possible latitudinal dependence of the altitude of the O peak density. Fig. 8 shows the altitude of the oxygen maximum averaged over 10 degree wide latitude bins. The vertical bars indicate the 1-σ dispersion about the mean value in each bin. The plot shows that no statistical dependence on latitude is observed, as confirmed by a linear correlation coefficient of 0.11. A large variability is seen at each latitude with largest values poleward of 60° N. For example, northward of 70° the 1-σ scatter extends from 94 to 115 km. This result suggests that the strength of vertical transport carrying the O atoms into the chemical recombination region is quite variable but does not significantly depend on latitude. Finally, we examine whether the O peak density shows any statistical dependence on latitude. Fig. 9 shows the peak density values binned over 5 degrees of latitude as a function of latitude. In this case, a clear trend appears, indicating that the highest O densities are observed at low latitudes, whereas values poleward of 70° N are statistically about a factor of two smaller. The linear correlation coefficient r is equal to −0.83, although it is not necessarily expected that the oxygen density would vary linearly with latitude. As noted for the altitude of the O peak, the variability of the O density is larger at higher latitudes while the number of profiles in each bin is not significantly different. We note that this result is consistent with the concept that, on the average, the antisolar to subsolar circulation concentrates the downward flow of oxygen atoms toward low latitude regions (Bougher et al., 2006).

5. Comparison with one-dimensional model

We now compare the O vertical profiles obtained following inversion of the limb profiles and use of relation (4) with the results of one-dimensional modeling based on oxygen nightside photochemistry. The one-dimensional model, its photochemistry, vertical transport and numerical methods were described by Gérard et al. (2008b) and Cox et al. (2008). It solves the one-dimensional continuity equations (Bougher et al., 2006):

$$\partial n_i/\partial t = P_i - L_i - \partial \Phi_i/\partial z, \quad (6)$$

with $i = O(^3P)$, $N(^4S)$, NO, O_2 and $O_2(^1\Delta_g)$, using a finite volume method, with P_i and L_i the chemical production and loss rates, respectively, and Φ_i the vertical flux of the ith component. In addition to reaction (1), radiative recombination of O atoms with N:

$$O + N \rightarrow NO \quad (7)$$

is a secondary loss of O. The upper and lower boundaries are set at 130 and 80 km, respectively. A downward flux of O and N atoms is allowed to flow through the upper boundary the atoms are transported into the chemical loss region by molecular and eddy diffusion where they are lost through reactions (1) and (7). The constituents are assumed to be in photochemical equilibrium at the lower boundary. The rate coefficients are based on the discussion by Slanger et al. (2006). The temperature and densities profiles of the background constituents vertical are taken from Hedin et al. (1983). Below the homopause, vertical transport is parameterized by an eddy diffusion coefficient in the form $An^{-1/2}$ where A is an empirically estimated coefficient and n is the total number density in cm^{-3}. The altitude of the peak of the 1.27-μm emission depends on the strength of eddy mixing and the brightness depends on the downward flux of O atoms through the upper boundary. Fig. 10 illustrates the comparison between the O density derived from Abel inversion of the $O_2(^1\Delta)$ limb profile observed on orbit 383 near midnight at 26° N, and the result of the one-dimensional model calculation best fitting the airglow profile. The error bars indicate the uncertainty on the O density generated by the Abel inversion algorithm. It is on the order of 3% at the peak, increasing up to 50% at 117 km. In the model simulation, the O downward flux is 1.3×10^{12} $cm^{-2}\,s^{-1}$ at 130 km and the A coefficient of the eddy

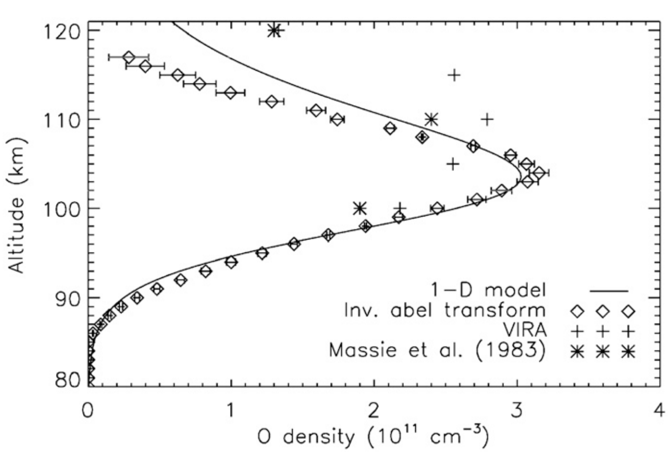

Fig. 10. Oxygen density profile derived from an airglow limb profile observed on orbit 383 at 2354 LT at a latitude of 26° N and distribution calculated with the one-dimensional chemical-diffusive model. For comparison, nightside values from Massie et al. (1983) and from the VIRA model for midnight and 0° latitude are also shown.

diffusion coefficient 2.2×10^{13}. The bottomside and peak value of the O layer are well reproduced by the one-dimensional model. The equatorial values calculated for 0000 LT by Massie et al. (1983) and the nightside VIRA (Keating et al., 1985) profile are shown for comparison. In this particular case, the O distribution derived from the airglow profile shows a peak of 3.1×10^{11} cm^{-3}, compared to 2.8×10^{11} cm^{-3} for the VIRA nightside profile. The maximum O density is located at 103 km, 7 km below the VIRA profile.

6. Discussion and conclusions

Observations by VIRTIS of $O_2(^1\Delta_g)$ emission provide a powerful method to investigate the coupling between global and local transport and photochemistry in the Venus nightside mesosphere and lower thermosphere. Early results indicated that the airglow layer is usually located near 97 ± 2 km and shows patchy structures with considerable variability over timescales of a few hours or days. Analysis of nadir images shows that both the global subsolar to antisolar circulation systems and zonal winds combine in a complex way to generate the observed structures and apparent transport of airglow clouds. Correlations between the airglow brightness and local temperatures determined by VIRTIS (Piccioni et al., 2008) suggest the presence of regions of enhanced or suppressed downward flow of atomic oxygen atoms. The global picture emerging from these observations is therefore considerably more complex than previously thought. The distribution of atomic oxygen in the nightside upper mesosphere and its variability are reflected by the behavior of the infrared O_2 airglow.

In this study, we have shown that the mechanism leading to the production of the $O_2(^1\Delta_g)$ emission is well understood and that airglow limb profiles may be used to derive the O distribution in the 90–115 km region. In particular, use of the CO_2 density distribution deduced from analysis of concurrent stellar occultation profiles reduces the uncertainties on the oxygen density. We have shown, that if a CO_2 mean profile is adopted instead, the error on the O peak density is on the order of 30%. Observed latitudinal distributions of vertical O profiles obtained by Abel inversion show changes in both the altitude and the magnitude of the oxygen peak, sometimes over only a few degrees, in agreement with the sharp structures occasionally observed in nadir images. Typical maximum O densities vary between 1×10^{11} and 5×10^{11} cm^{-3} with peaks located in the 95 to 115 km range. As discussed before, the Abel inversion method used in this study is unable to derive O profiles in regions of sharp horizontal gradient where limb profiles are integrated over regions corresponding to widely different vertical airglow distributions.

The O densities deduced from this study are in general agreement with the VIRA midnight profile, which is largely based on the vertical distribution modeled by Massie et al. (1983). The VIRA profile shows a peak of 3×10^{11} cm^{-3} at 110 km. However, the mean altitude of the maximum O density derived from the 1.27 μm airglow is ~104 km, 6 km lower than VIRA and the peak density is 2.2×10^{11} cm^{-3} (averaged over local times). No statistical latitudinal dependence of the altitude of the O is deduced but the maximum density drops by a factor of two from low to high latitudes. As discussed before, in addition to the Abel inversion, one source of uncertainty on O density is the CO_2 profile used in relation (4). To a minor extent, other uncertainties include the rate coefficient k, the efficiency ε of the three-body recombination (1) with CO_2 as a third body and the quenching coefficient of $O_2(^1\Delta_g)$ by CO_2. Experimental determination of both quantities is desirable. We note that (i) reaction (1) is the dominant chemical sink of O atoms on the nightside, (ii) evidence indicates that the efficiency ε is close to unity and (iii) the value of the quenching coefficient C used in (4) is an upper limit. Increasing the efficiency ε from 0.75 to 1 decreases the O densities by only 15%. If the quenching coefficient C is significantly less than 2×10^{-20} $cm^3 s^{-1}$, the derived O density increases by ∼20% at 95 km, 5% at 100 km and remains practically unaffected at higher altitude.

We conclude that the O_2 infrared night airglow provides a power tool to remotely map the global distribution of atomic oxygen in the Venus mesosphere between ∼90 and 115 km. Future studies with wider coverage will examine possible local time and solar activity effects on the atomic oxygen distribution. It is expected that the global distribution of atomic oxygen on the Venus nightside will be globally mapped and integrated into future empirical models of the Venus atmosphere.

Acknowledgments

We gratefully thank all members of the ESA Venus Express project and of the VIRTIS (http://servirtis.obspm.fr/Venus_Express/VIRTIS_Team.html) and SPICAV scientific and technical teams J.C.G. acknowledges funding from the Belgian Fund for Scientific Research (FNRS). A. Saglam is supported the PRODEX program managed the European Space Agency with the help of the Belgian Federal Space Science Policy Office. This work is supported by Agenzia Spaziale Italiana and the Centre National d'Etudes Spatiales.

References

Allen, D., Crisp, D., Meadows, V., 1992. Variable oxygen airglow on Venus as a probe of atmospheric dynamics. Nature 359, 516–519.

Bates, D.R., 1988. Excitation and quenching of the oxygen bands in the nightglow. Planet. Space Sci. 36, 875–881.

Bertaux, J.-L., Vandaele, A.-C., Korablev, O., Villard, E., Fedorova, A., Fussen, D., Quémerais, E., Belyaev, D., 2007. A warm layer in Venus' cryosphere and high-altitude measurements of HF, HCl, H_2O and HDO. Nature 450, 646–649.

Bougher, S.W., Borucki, W.J., 1994. Venus O_2 visible and IR nightglow: Implications for lower thermosphere dynamics and chemistry. J. Geophys. Res. 99, 3759–3776.

Bougher, S.W., Rafkin, S., Drossart, P., 2006. Dynamics of the Venus upper atmosphere: Outstanding problems and new constraints expected from Venus Express. Planet. Space Sci. 54, 1371–1380.

Campbell, I.M., Gray, C.N., 1973. Rate constants for the $O(^3P)$ recombination and association with $N(^4S)$. Chem. Phys. Lett. 18, 607–609.

Connes, P., Noxon, J.F., Traub, W.A., Carleton, N.P., 1979. $O_2(^1\Delta)$ emission in the day and night airglow of Venus. Astrophys. J. 233, L29–L32.

Cox, C., Saglam, A., Gérard, J.-C., Bertaux, J.-L., González-Galindo, F., Leblanc, F., Reberac, A., 2008. The distribution of the ultraviolet nitric oxide martian night airglow: Observations from Mars Express and comparisons with a one-dimensional model. J. Geophys. Res. 113. E08012.

Crisp, D., Meadows, V.S., Bézard, B., de Bergh, C., Maillard, J.-P., Mills, F.P., 1996. Ground-based near-infrared observations of the Venus nightside: 1.27-μm $O_2(a^1\Delta g)$ airglow from the upper atmosphere. J. Geophys. Res. 101, 4577–4594.

Drossart, P., Bézard, B., Encrenaz, Th., Lellouch, E., Roos, M., Taylor, F.W., Collard, A.D., Calcutt, S.B., Pollack, J., Grinspoon, D.H., Carlson, R.W., Baines, K.H., Kamp, L.W., 1993. Search for spatial variations of the H_2O abundance in the lower atmosphere of Venus from NIMS-Galileo. Planet. Space Sci. 41, 495–504.

Drossart, P., and 43 colleagues, 2007a. Scientific goals for the observation of Venus by VIRTIS on ESA/Venus Express mission. Planet. Space Sci. 55, 1653–1672.

Drossart, P., and 43 colleagues, 2007b. Infrared spectral imaging observations of Venus by VIRTIS reveal a dynamical upper atmosphere. Nature 450, 641–645.

Gérard, J.-C., Stewart, A.I.F., Bougher, S.W., 1981. The altitude distribution of the Venus ultraviolet airglow and implications on vertical transport. Geophys. Res. Lett. 8, 633–636.

Gérard, J.-C., Saglam, A., Piccioni, G., Drossart, P., Cox, C., Erard, S., Hueso, R., Sanchez-Lavega, A., 2008a. Distribution of the O_2 infrared nightglow observed with VIRTIS on board Venus Express. Geophys. Res. Lett. 35. L02207.

Gérard, J.-C., Cox, C., Saglam, A., Bertaux, J.-L., Villard, E., Nehmé, C., 2008b. Limb observations of the ultraviolet nitric oxide nightglow with SPICAV on board Venus Express. J. Geophys. Res. 113. E00B03.

Hedin, A.E., Niemann, H.B., Kasprzak, W.T., Seiff, A., 1983. Global empirical model of the Venus thermosphere. J. Geophys. Res. 88, 73–83.

Hueso, R., Sanchez-Lavega, A., Piccioni, G., Drossart, P., Gérard, J.-C., Khatuntsev, I., Zasova, L., Migliorini, A., 2008. Morphology and dynamics of Venus oxygen airglow from Venus Express/VIRTIS observations. J. Geophys. Res. 113, doi:10.1029/2008JE003081. E00B02.

Kasprzak, W.T., Hedin, A.E., Mayr, H.G., Niemann, H.B., 1988. Wavelike perturbations in the neutral atmosphere of Venus. J. Geophys. Res. 93, 11237–11245.

Kasprzak, W.T., Niemann, H.B., Hedin, A.E., Keating, M.G., Bougher, S.W., Hunten, D.M., 1993. Neutral composition measurements by the Pioneer Venus neutral mass spectrometer during orbiter re-entry. Geophys. Res. Lett. 20, 2747–2750.

Keating, G.M., Bertaux, J.L., Bougher, S.W., Dickinson, R.E., Cravens, T.E., Hedin, A.E., 1985. Venus international reference atmosphere. Adv. Space Res. 5, 117–171.

Krasnopolsky, V.A., 1986. Oxygen emissions in the night airglow of the Earth, Venus, and Mars. Planet. Space Sci. 34, 511–518.

Krasnopolsky, V.A., Parshev, V.A., 1983. Photochemistry of the Venus atmosphere. In: Hunten, D.M., Colin, L., Donahue, T.M., Moroz, V.I. (Eds.). Venus. Univ. of Arizona Press, Tucson, pp. 431–458.

Lellouch, E., Clancy, T., Crisp, D., Kliore, A., Titov, D., Bougher, S.W., 1997. Monitoring of mesospheric structure and dynamics. In: Bougher, S.W., Hunten, D.M., Philips, R.J. (Eds.), Venus. II. Geology, Geophysics, Atmosphere, and Solar Wind Environment. Univ. of Arizona Press, Tucson, p. 295.

Leu, M.T., Yung, Y.L., 1987. Determination of the $O_2(^1D)$ and $O_2(^1S)$ yields in the reaction $O + ClO = Cl + O_2$: Implications for photochemistry in the atmosphere of Venus. Geophys. Res. Lett. 14, 949–952.

Massie, S.T., Hunten, D.M., Sowell, D.T., 1983. Day and night models of the Venus thermosphere. J. Geophys. Res. 88, 3955–3969.

Mayr, X., Harris, H.G., Kasprzak, W.T., Dube, M., Varosi, F., 1988. Gravity waves in the upper atmosphere of Venus. J. Geophys. Res. 93, 11,247–11,262.

Miller, H.C., McCord, J.E., Choy, J., Hager, G.D., 2001. Measurement of the radiative lifetime of $O_2(a^1\Delta_g)$ using cavity ring down spectroscopy. J. Quant. Spectrosc. Radiat. Trans. 69, 305–325.

Montmessin, F., and 10 colleagues, 2006a. Sub-visible CO_2 ice clouds detected in the mesosphere of Mars. Icarus 183, 403–410.

Montmessin, F., Quémerais, E., Bertaux, J.L., Korablev, O., Rannou, P., Lebonnois, S., 2006b. Stellar occultations at UV wavelengths by the SPICAM instrument: Retrieval and analysis of martian haze profiles. J. Geophys. Res. 111. E09S09.

Nair, H., Allen, M., Anbar, A.D., Yung, Y.L., Clancy, R.T., 1994. A photochemical model of the martian atmosphere. Icarus 111, 124–150.

Niemann, H.B., Kasprzak, W.T., Hedin, A.E., Hunten, D.M., Spencer, N.W., 1980. Mass spectrometric measurements of the neutral gas composition of the thermosphere and exosphere of Venus. J. Geophys. Res. 85, 7817–7827.

Parkinson, W.H., Rufus, J., Yoshino, K., 2003. Absolute cross section measurements of CO_2 in the wavelength region 163–200 nm and the temperature dependence. Chem. Phys. 219, 45–57.

Piccioni, G., Zasova, L., Migliorini, A., Drossart, P., Shakun, V., García Muñoz, V., Mills, F.P., Cardesin, A., and the VIRTIS-Venus Express Team, 2008. Oxygen nightglow vertical distribution from the VIRTIS Near IR observations in the Venus upper atmosphere. J. Geophys. Res., submitted for publication.

Quémerais, E., Bertaux, J.-L., Korablev, O., Dimarellis, E., Cot, C., Sandel, B.R., Fussen, D., 2006. Stellar occultations observed by SPICAM on Mars Express. J. Geophys. Res. 111. E09 S04.

Sander, S.P., and 10 colleagues, 2003. Chemical kinetics and photochemical data for use in atmospheric studies, Evaluation number 14, JPL publication 02-25.

Slanger, T., Huestis, D.L., Cosby, P.C., Chanover, N.J., Bida, T.A., 2006. The Venus nightglow ground-based observations and chemical mechanisms. Icarus 182, 1–9.

Svedhem, H., and 26 colleagues, 2007. Venus Express—The first European mission to Venus. Planet. Space Sci. 55, 1636–1652.

Titov, D.V., and 22 colleagues, 2006. Venus Express science planning. Planet. Space Sci. 54, 1279–1297.

Von Zahn, U., Fricke, K.H., Hunten, D.M., Krankowsky, D., Mauersberger, K., Nier, A.O., 1980. The upper atmosphere of Venus during morning conditions. J. Geophys. Res. 85, 7829–7840.

Yoshino, K., Esmond, J.R., Sun, Y., Parkinson, W.H., Ito, K., Matsui, T., 1996. Absorption cross section measurements of carbon dioxide in the wavelength region 118.7 nm–175.5 nm and the temperature dependence. J. Quant. Spectrosc. Radiat. Trans. 50, 53–60.

Yung, Y.L., DeMore, W.B., 1982. Photochemistry of the stratosphere of Venus: Implications for atmospheric evolution. Icarus 51, 199–247.